Available online at www.sciencedirect.com
SCIENCE DIRECT®
International Journal of Heat and Mass Transfer 48 (2005) 5475–5487
International Journal of HEAT and MASS TRANSFER
www.elsevier.com/locate/ijhmt

Numerical investigation of the air flow through a bundle of IP-SOFC modules

B.A. Haberman *, J.B. Young

Hopkinson Laboratory, Engineering Department, Cambridge University, Cambridge CB2 1PZ, UK

Received 15 October 2004
Available online 26 September 2005

Abstract

The integrated-planar solid oxide fuel cell (IP-SOFC) consists of ceramic modules which have electrochemical cells printed on the outer surfaces. The cathodes are the outermost layer of each cell and are supplied with oxygen from air flowing over the outside of each module. The anodes are in direct contact with the ceramic structure and are supplied with fuel from internal gas channels. An IP-SOFC power plant will contain many modules closely packed together in an array inside a pressure vessel. The air flow is also used to cool the modules. This paper describes a three-dimensional numerical method for simulating the air flow. It uses an explicit time-marching scheme that incorporates a preconditioning method to increase the rate of numerical convergence at low flow velocities. The numerical method is used to simulate the air flow through an array of IP-SOFC modules. The scheme is straightforward to implement and can predict the recirculating flows existing between the modules within an array. The calculation procedure is used to investigate the effect of different sized gaps between modules on the local heat and mass transfer coefficients. The results show the effect of the module arrangement on the flow field and how increasing the gap between modules improves the heat and mass transfer at the module surfaces.

Keywords: SOFC; Air flow; Simulation; Mass transfer; Heat transfer; Low Mach number

1. Introduction

The solid oxide fuel cell (SOFC) represents a new alternative to conventional methods of power generation as electric power is generated directly from the electrochemical oxidation of the fuel. The SOFC has several advantages over conventional systems including zero emissions of nitrogen and sulphur oxides. It also has a very high cycle efficiency when combined with a gas turbine.

The overall reaction that takes place within a fuel cell is the electrochemical oxidation of hydrogen

$$H_2 + \frac{1}{2}O_2 \rightarrow H_2O \quad (1)$$

The fuel and oxidant are separated by a semi-permeable solid electrolyte that can only transport oxygen ions. The overall electrochemical reaction can be decomposed into two half cell reactions as shown in Fig. 1. O_2 gas diffuses through the cathode and the electrochemical reaction,

* Corresponding author.
E-mail addresses: b.haberman.01@cantab.net (B.A. Haberman), jby@eng.cam.ac.uk (J.B. Young).

0017-9310/$ - see front matter © 2005 Elsevier Ltd. All rights reserved.
doi:10.1016/j.ijheatmasstransfer.2005.06.018

Nomenclature

c_p	constant pressure specific heat capacity
D	binary diffusion coefficient
e	specific energy
g	mass flux vector
G	total mass flux vector
h	specific enthalpy
L	computational domain dimension
M	module dimension
n	number of species
p	pressure
q	heat flux vector
R	specific gas constant
S	air gap dimension
s	surface area vector
t	time
T	temperature
U	velocity vector
V	volume
X	mole fraction
Y	mass fraction

Greek symbols

λ	thermal conductivity
μ	dynamic viscosity
ρ	density

Subscripts

i	component species i
m	mixed-mean
n	vector component normal to a surface
0	stagnation
ref	reference value
cell	cell-centred

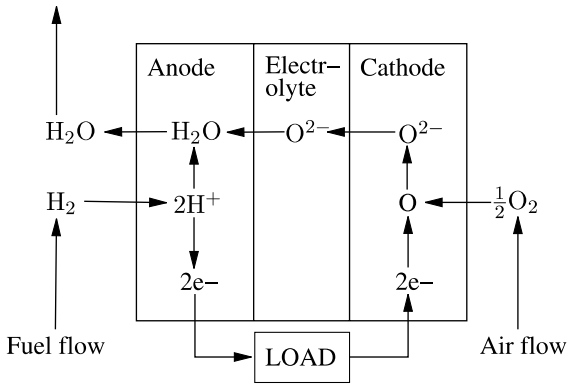

Fig. 1. Gas and ion transport and electrochemical reactions in an IP-SOFC.

$$\frac{1}{2}O_2 + 2e^- \rightarrow O^{2-} \tag{2}$$

occurs at, or near, the cathode–electrolyte interface. The O^{2-} ions migrate across the electrolyte while H_2 gas diffuses through the anode layers. The electrochemical reactions

$$H_2 \rightarrow 2H^+ + 2e^- \tag{3}$$

$$2H^+ + O^{2-} \rightarrow H_2O \tag{4}$$

occur at, or near, the anode–electrolyte interface and the reaction product H_2O diffuses back into the fuel channel. The solid oxide electrolyte material can only transport oxygen ions at high temperatures (>1073 K). However, material degradation can occur if the temperature increases beyond the operating limits and cooling of the cells is therefore of critical importance. This is achieved by heat transfer to the air flowing over the cathode.

The integrated-planar solid oxide fuel cell (IP-SOFC) is a recent design, pioneered by Rolls-Royce [1], which is currently creating great interest in the fuel cell community. As shown in Fig. 2 the electrochemical cells of an IP-SOFC are fabricated on the outside of the ceramic module material. The anodes are printed directly onto the module surface and are supplied with fuel from the internal gas channels. The cathode is the outermost layer of each cell and is supplied with oxygen from the air flowing over the outside of the module. The air flow also provides forced convection cooling. The performance of each electrochemical cell depends both on its temperature and the partial pressure of oxygen at the cathode surface. Hence, it is important to be able to predict these properties within the flow field.

For the purposes of this study, the IP-SOFC modules are treated as flat plates with heat and mass flux boundary conditions on their surfaces. This is acceptable because the electrochemical cells are very thin and the air flow is laminar. Analytical solutions exist for developing thermal and diffusion boundary layers on flat plates with constant heat and mass flux boundary conditions [2]. The boundary layers thicken as the flow develops within the air channel and eventually become fully-developed. The heat and mass transfer coefficients are infinite at the leading edges of the plates and decrease rapidly toward constant fully-developed values. The analysis also shows that for gases such as air (where the Prandtl and Schmidt numbers are nearly of equal magnitude) an analogy can be made between heat and mass transfer because the thermal and diffusion boundary layers exhibit very similar behaviour.

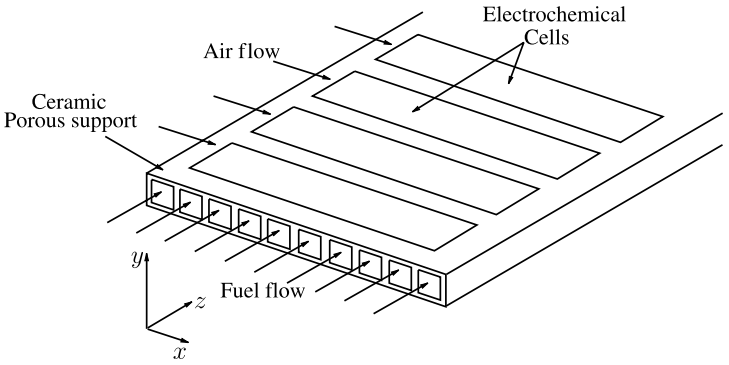

Fig. 2. The Rolls-Royce IP-SOFC, schematic diagram of a module. The electrochemical cells are printed on both sides of the ceramic structure.

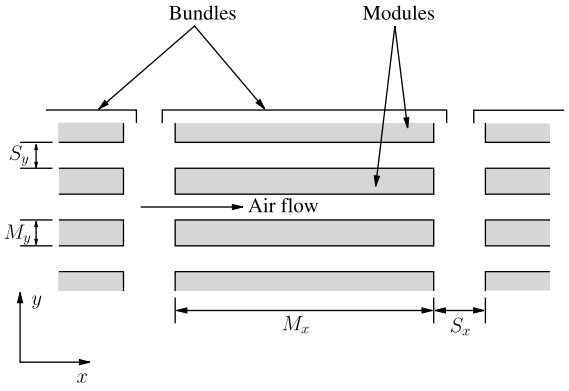

Fig. 3. Schematic diagram of an array of bundles of modules.

An IP-SOFC power system will consist of a pressure vessel, inside which are closely packed modules arranged in groups or 'bundles'. Fig. 3 shows a cross-section through an array of bundles in the x–y plane. Air will be blown in the x-direction through the gaps (S_y) between modules within a bundle and will flow from one bundle to the next via the gaps (S_x) between bundles. It is assumed that there are no gaps between bundles or modules in the z-direction and hence the geometry is two-dimensional. There is a large body of work on the design of heat exchangers and cooling fins that consist of arrays of flat plates similar to Fig. 3 [3–7]. Heat transfer can be improved by increasing the flow rate of the cooling fluid or by altering the arrangement of the plates. The gaps between plates in the flow direction (S_x) serve to break up the boundary layers leading to improved heat transfer at the leading edge of each successive plate. There are several Reynolds numbers Re that characterise the air flow regime through an array of flat plates. They have the general form

$$Re_d = \frac{\rho U_m d}{\mu}$$

where U_m is the mean air velocity between the parallel plates, ρ is the density of the gas, μ is the dynamic viscosity and d is the characteristic length. The Reynolds number Re_S is based on a characteristic length of $2S_y$, the hydraulic diameter of two plates with a separation of S_y. The Reynolds number Re_M uses a characteristic length of $M_y/2$, the half-thickness of a module in the y-direction. For the operating conditions and geometry considered in this study, $Re_S \approx 100$ and $Re_M \approx 50$. At low values of Re_S and Re_M the air flow is expected to be steady and laminar. As Reynolds number increases the flow regime can become unsteady and three-dimensional behaviour can exist despite the two-dimensional nature of the geometry. Zhang et al. [7] investigated the air flow through an array of flat plates using both steady and unsteady numerical simulations at different values of Reynolds number (Re_{Zh}, described in the study). The results obtained agreed well with experimental data and showed that the flow regime remained steady and two-dimensional for $Re_{Zh} \leqslant 350$ ($Re_{Zh} \leqslant 100$ for the operating conditions and geometry used in this study). The onset of three-dimensional flow behaviour was found to occur only once the flow had become unsteady. Zhang et al. [7] also showed that the steady flows were symmetric about the x-axis of each plate and accurate results could be obtained from a computational domain halved in size along this line of symmetry.

This paper describes a three-dimensional numerical method used to predict the behaviour of the steady laminar air flow over the outside of IP-SOFC modules arranged in an array. Although not discussed here, the numerical method is also suitable for the simulation of the fuel flow inside the modules where large changes in gas composition and temperature occur due to chemical reaction and diffusion [8]. There are many different approaches to the numerical solution of the Navier–Stokes equations. This paper is concerned with an explicit time-marching method, where time is a

pseudo-variable used to facilitate convergence to a steady-state solution.

Explicit time-marching methods for compressible flows are straightforward to implement and converge rapidly to the steady-state solution at high Mach numbers. However, at IP-SOFC operating conditions, the mean air velocity over an array of modules is expected to be around 2.5 m s^{-1} which equates to a Mach number of 0.004. Air behaves almost incompressibly at such a low Mach number and this can present problems for a numerical solution method. At low Mach numbers the convective speed is much smaller than the acoustic speed and hence the convective part of the solution requires much larger time steps than the acoustic part to converge quickly. The allowable stable time step is dictated by the maximum speed at which information can travel through the flow field, i.e. by the acoustic speed. Hence, the stable time steps are too small for the convective part of the solution to converge quickly at low Mach numbers. Several numerical methods have been developed to address this problem [9–14]. One attractive approach is to solve the compressible flow equations with preconditioned time derivatives. Weiss and Smith [11] multiplied the time derivatives by a preconditioning matrix which forced the acoustic and convective speeds to be of the same order of magnitude and the convergence times using this method were found to be independent of Mach number. An alternative approach is to assume the gas flow is incompressible and to vary density or pressure artificially with time thus providing 'pseudo-compressibility'. Kwak and Chakravarthy [14] used this method to predict various three-dimensional flow fields.

This paper describes a numerical scheme which uses a simplified version of the 'preconditioning' method and is suitable for simulating the IP-SOFC flow fields described above. The results are validated against several test cases and an investigation into the effects of 'bundle geometry' is also described.

2. The physical model

2.1. General description

Fig. 2 shows the geometry of one end of an IP-SOFC module. A module has up to 20 cells printed on the top and bottom faces, covering roughly half the available surface area. For the purposes of this study, it is assumed that there is one large cell covering the whole of the top and bottom faces and the boundary conditions on the module surface are adjusted accordingly. The modules are assumed to be arranged in an array that repeats infinitely in all directions (see Fig. 3). The module outer dimensions used for this study are $M_x = 60$ mm in the x-direction, $M_y = 6$ mm in the y-direction and $M_z = 400$ mm in the z-direction. In this study the air gap between modules S_y is fixed at 3 mm and the gap between bundles S_x is varied from 5 mm to 25 mm. The mean velocity of the air flow between modules is fixed at 2.5 m s^{-1}. Fig. 4 shows a cross-section showing the computational domain in an x–y plane located at $z = M_z/2$ and the coordinate system used throughout this paper. The size of the domain is reduced to the smallest repeating unit that describes the geometry by using the lines of symmetry that exist, including the x-axis of each plate. The computational domain has a varying dimension L_x in the x-direction, $L_y = 4.5$ mm in the y-direction and $L_z = 400$ mm in the z-direction.

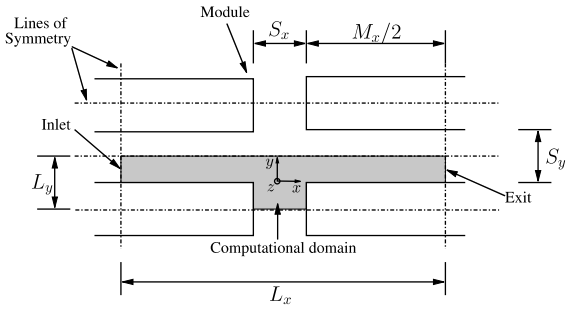

Fig. 4. Cross-section showing the computational domain.

2.2. Boundary conditions

Adiabatic slip boundary conditions are applied to the domain boundaries which lie on the horizontal lines of symmetry and to the domain side walls ($z = 0$ and $z = L_z$ boundaries, not shown). The inlet boundary is set using the distribution of gas properties at the outlet boundary which has been adjusted to have the specified mean inlet values of stagnation pressure $p_{0,m}$, stagnation temperature $T_{0,m}$ and component gas mole fractions $X_{i,m}$. A value of static pressure p is specified at the outlet boundary to give the desired mean velocity through the domain. The electrochemical cells are accounted for by specifying appropriate heat and mass flux boundary conditions at the top face of the module ($y = 0$). The front and back faces of the module ($x = S_x/2$, $x = -S_x/2$) have no electrochemical cells printed on them and so there is a zero mass flux boundary condition. However, the front and back faces are not adiabatic because the module conducts heat. Therefore, it is assumed that the temperatures of the front and back faces are fixed at the temperatures of the adjacent edges of the top face. A no-slip boundary condition is applied to all the module faces.

The electric current density in each cell is assumed to be uniform at 300 mA cm^{-2} and hence a value of 150 mA cm^{-2} is used for the entire module surface.

Table 1
Boundary conditions

Location	Boundary condition
$y = 0$ (module top surface)	$G_{y,O_2} = -0.109\ \text{g s}^{-1}\ \text{m}^{-2}$ $G_{y,N_2} = 0.0$ $q_y = 625\ \text{W m}^{-2}$
$x = -S_x/2$ (module back wall)	$G_x = 0.0$ $T(x, y) = T(x, 0)$
$x = S_x/2$ (module front wall)	$G_x = 0.0$ $T(x, y) = T(x, 0)$
$y = S_y/2$ (channel centreline)	$G_y = 0.0$ $q_y = 0.0$
$z = 0$, $z = L_z$ (domain end walls)	$G_z = 0.0$ $q_z = 0.0$
$x = -L_x/2$ (inlet)	$p_{0,m} = 100000\ \text{Pa}$ $T_{0,m} = 1123\ \text{K}$ $X_{N_2,m} = 0.79$ $X_{O_2,m} = 0.21$
$x = L_x/2$ (outlet)	$p = 99990\ \text{Pa}$

The corresponding rate of oxygen consumption at the cathode surface can then be deduced from Eq. (2). The heat flux from the module surface is set to $625\ \text{W m}^{-2}$ which represents a typical heat production of 30 W per module. The gas composition fixed at the inlet is an oxygen/nitrogen mixture representative of air. The heat fluxes and total mass fluxes normal to the boundary surfaces (q_n, $G_{n,i}$) and the inlet and outlet boundary conditions used for the simulation are all given in Table 1.

3. The governing equations

The equations presented here are for an unsteady three-dimensional, low Mach-number, compressible flow.

3.1. Conservation of momentum

An equation can be written for the conservation of momentum in each direction, shown here in the x-direction,

$$\frac{\partial \rho U_x}{\partial t} + \left[\frac{\partial \rho U_x U_x}{\partial x} + \frac{\partial \rho U_y U_x}{\partial y} + \frac{\partial \rho U_z U_x}{\partial z}\right] = \left[-\frac{\partial p}{\partial x} + \frac{\partial \tau_{xx}}{\partial x} + \frac{\partial \tau_{xy}}{\partial y} + \frac{\partial \tau_{xz}}{\partial z}\right] \tag{5}$$

where ρ is the density of the gas mixture, U_x is the component of the velocity vector $\mathbf{U}$ in the x-direction and p is the pressure. The shear stresses τ_{xx}, τ_{xy} and τ_{xz} are given by

$$\tau_{xx} = 2\mu\frac{\partial U_x}{\partial x} - \frac{2}{3}\mu\left(\frac{\partial U_x}{\partial x} + \frac{\partial U_y}{\partial y} + \frac{\partial U_z}{\partial z}\right) \tag{6}$$

$$\tau_{xy} = \mu\left(\frac{\partial U_y}{\partial x} + \frac{\partial U_x}{\partial y}\right) \tag{7}$$

$$\tau_{xz} = \mu\left(\frac{\partial U_x}{\partial z} + \frac{\partial U_z}{\partial x}\right) \tag{8}$$

where μ is the dynamic viscosity of the gas. The transition to a natural convection dominated flow regime occurs if the Grashof number (Gr) is much greater than the smallest Reynolds number squared, Re_M^2. In this study Gr is defined as

$$Gr = \frac{g\Delta T \rho^2 (2S_y)^3}{T\mu^2} \tag{9}$$

where g is the acceleration due to gravity and T is the temperature of the gas. If the value of temperature difference ΔT is chosen to represent the most favourable conditions for promoting natural convection, the maximum value of Gr/Re_M^2 is about 0.01. Therefore, it can be assumed that forced convection will dominate and a buoyancy term is not included in Eq. (5).

3.2. Conservation of species

A conservation equation can be written for each of the two gas species

$$\frac{\partial \rho_i}{\partial t} + \nabla \cdot \mathbf{G}_i = 0 \tag{10}$$

where ρ_i is the density of species i. The total flux vector of the ith species $\mathbf{G}_i$ is the sum of the convection and diffusion fluxes

$$\mathbf{G}_i = \rho_i \mathbf{U} + \mathbf{g}_i \tag{11}$$

where the mass-averaged velocity $\mathbf{U}$ is the velocity calculated from the momentum equations (5) and $\mathbf{g}_i$ is the diffusion mass flux relative to the mass-averaged velocity. For a binary system, the diffusion mass fluxes can be calculated in a straightforward manner by the expression

$$\mathbf{g}_i = -\rho D \nabla Y_i \tag{12}$$

where Y_i is the mass fraction of species i and D is the binary diffusion coefficient of a mixture of O_2 and N_2.

3.3. Conservation of energy

The equation describing the conservation of energy is,

$$\frac{\partial(\rho e)}{\partial t} = -\nabla \cdot \left(\rho \mathbf{U}\left(h + \frac{1}{2}\mathbf{U}^2\right)\right) + \nabla \cdot (\lambda \nabla T) - \nabla \cdot \left(\sum_{i=1}^{n} \mathbf{g}_i h_i\right) \tag{13}$$

where e is the specific energy, h is the specific enthalpy and λ is the thermal conductivity, all of the gas mixture. The final term on the right represents the enthalpy flux due to diffusion. h_i is the partial enthalpy of the ith species and is calculated from

$$h_i = \int_{T_d}^{T} c_{p_i}(T^*)\mathrm{d}T^* \tag{14}$$

where $T_d = 298.15$ K, the datum temperature. Eq. (14) holds because the enthalpy of formation at 298.15 K of both O_2 and N_2 is zero. The specific enthalpy of the gas h is then given by

$$h = \sum_{i=1}^{n} Y_i h_i \tag{15}$$

and the specific energy of the gas e is given by

$$e = h + \frac{1}{2}\mathbf{U}^2 - RT \tag{16}$$

where R is the specific gas constant for the gas mixture.

4. The numerical scheme

4.1. General description

The conservation equations are solved using a finite volume time-marching method on a structured rectangular grid with variables stored at cell vertices, see Fig. 5. It should be noted that the numerical solution method is not currently time-accurate and time is used as a pseudo-variable simply to facilitate convergence to the steady-state solution. Variable grid spacings are used to create a finer grid near the domain boundaries to capture boundary layer effects. This code is based on a code originally developed for compressible turbomachinery calculations by Denton [15].

In order to maintain numerical accuracy at low Mach numbers ($M < 0.01$) it is necessary to non-dimensionalise the governing equations. A set of reference terms, denoted by the subscript 'ref', are used to non-dimensionalise all the terms in the governing equations as follows:

$$\begin{aligned}
x' &= \frac{x}{L_{\mathrm{ref}}} & h' &= \frac{h}{U_{\mathrm{ref}}^2} \\
\mathbf{U}' &= \frac{\mathbf{U}}{U_{\mathrm{ref}}} & R' &= R\frac{T_{\mathrm{ref}}}{U_{\mathrm{ref}}^2} \\
\rho' &= \frac{\rho}{\rho_{\mathrm{ref}}} & C_p' &= C_p\frac{T_{\mathrm{ref}}}{U_{\mathrm{ref}}^2} \\
T' &= \frac{T}{T_{\mathrm{ref}}} & p' &= \frac{p}{\rho_{\mathrm{ref}}U_{\mathrm{ref}}^2} \\
t' &= \frac{t\,U_{\mathrm{ref}}}{L_{\mathrm{ref}}} & \mu' &= \frac{\mu}{\rho_{\mathrm{ref}}U_{\mathrm{ref}}L_{\mathrm{ref}}} \\
e' &= \frac{e}{U_{\mathrm{ref}}^2} & \lambda' &= \frac{\lambda T_{\mathrm{ref}}}{\rho_{\mathrm{ref}}U_{\mathrm{ref}}^3L_{\mathrm{ref}}}
\end{aligned} \tag{17}$$

In Eq. (17) the reference terms represent the mean flow field properties and the minimum domain dimension at the inlet boundary and $'$ represents a non-dimensionalised variable. U_{ref}^2 is used to non-dimensionalise the energy terms so the form of the equations remains unchanged. All the equations in this paper are represented in dimensional form for clarity. The equations are discretized using a control volume approach for each computational grid cell to provide an estimate of the time rate of change of each primary variable in the centre of each cell,

$$\left(\frac{\partial\rho_i}{\partial t}\right)_{\mathrm{cell}} = \frac{1}{V}\left[-\int_{\mathbf{s}}(Y_i\rho\mathbf{U} + \mathbf{g}_i)\cdot\mathrm{d}\mathbf{s}\right] \tag{18}$$

$$\begin{aligned}
\left(\frac{\partial\rho U_x}{\partial t}\right)_{\mathrm{cell}} = \frac{1}{V}\Bigg[&-\int_{s_x}\left(\rho U_x^2 + p - \tau_{xx}\right)\mathrm{d}s_x \\
&-\int_{s_y}\left(\rho U_y U_x - \tau_{xy}\right)\mathrm{d}s_y \\
&-\int_{s_z}\left(\rho U_z U_x - \tau_{xz}\right)\mathrm{d}s_z\Bigg]
\end{aligned} \tag{19}$$

$$\left(\frac{\partial\rho e}{\partial t}\right)_{\mathrm{cell}} = \frac{1}{V}\left[-\int_{\mathbf{s}}\left(\rho h\mathbf{U} - \lambda\nabla T + \sum_{i=1}^{n}\mathbf{g}_i h_i\right)\cdot\mathrm{d}\mathbf{s}\right] \tag{20}$$

where V is the volume of the grid cell, $\mathrm{d}s_x$ is the component of the cell surface vector $\mathbf{ds}$ in the x-direction and similarly for $\mathrm{d}s_y$ and $\mathrm{d}s_z$. The calculation of the fluxes through the cell surfaces is straightforward because of the cell-vertex storage scheme. All the first-order derivatives calculated at internal cell vertices within the computational domain are evaluated using central differences. The first-order derivatives required at cell vertices on the boundaries of the domain are calculated using one-sided differences. The stability of the scheme is improved by estimating the change in each primary

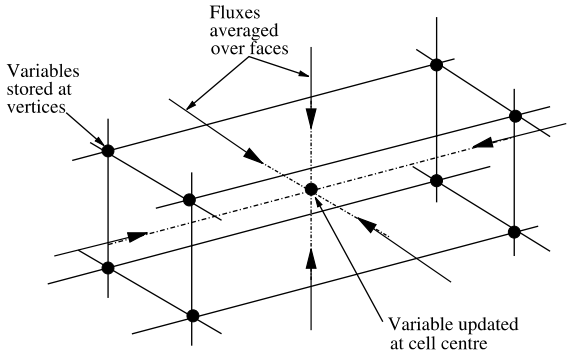

Fig. 5. Diagram showing a computational cell and the storage of information.

variable over a given time step using a second-order accurate method

$$(\Delta\rho_i)_{\text{cell}} = \left(\frac{\partial\rho_i}{\partial t}\right)_{\text{cell}}(\Delta t)_{\text{cell}} + \frac{1}{2}\left(\frac{\partial^2\rho_i}{\partial t^2}\right)_{\text{cell}}(\Delta t)^2_{\text{cell}} \tag{21}$$

$$(\Delta\rho_i)^n_{\text{cell}} = (\Delta t)^n_{\text{cell}}\left[\left(\frac{\partial\rho_i}{\partial t}\right)^n_{\text{cell}} + \frac{1}{2}\left[\left(\frac{\partial\rho_i}{\partial t}\right)^n_{\text{cell}} - \left(\frac{\partial\rho_i}{\partial t}\right)^{n-1}_{\text{cell}}\right]\right] \tag{22}$$

where the second-order time derivative is estimated from the difference between the first-order time derivatives stored at the current (n) and previous ($n-1$) time steps.

The allowable time step for each computational cell Δt_{cell} is estimated from the shortest time that information can travel across each cell and a CFL number,

$$\Delta t_{\text{cell}} = \text{CFL} \times \frac{d_{\min}}{U_{\max}}, \qquad U_{\max} = \sqrt{\gamma RT} \tag{23}$$

where for each computational grid cell, $d_{\min}$ is the minimum dimension and $\sqrt{\gamma RT}$ is the speed of sound. The pressure field at each time step is calculated from the ideal gas equation

$$p = \rho RT \tag{24}$$

where R is the specific gas constant and the density and temperature are updated using Eqs. (18) and (20) respectively. The convective flow field is found from the vector $\rho\mathbf{U}$ which is updated at each time step from Eq. (19). The calculation of the pressure field becomes unstable if the time steps are calculated using $\text{CFL} > 0.5$. The convergence time for a low Mach number flow can then become very large because the allowable time steps are far too small to allow rapid convergence of the convective flow field. However, there is very little pressure variation in a low Mach number flow and it is therefore not necessary to use a CFL number as large as 0.5 to obtain a solution for pressure. If the pressure is updated using $\text{CFL} = 0.005$ (1% of the maximum value), the stability of the system is improved and it is possible to update $\rho\mathbf{U}$, ρ_i and ρe at constant pressure over much larger time steps ($\text{CFL} = 8$).

This method of 'preconditioning' the time derivatives is used in conjunction with a multi-grid method to further increase the rate of convergence. The multi-grid method sums the flow property changes at each time step on three separate computational grids. The three grids vary in size from a grid that represents the entire computational domain with one large cell to a grid where each cell is represented individually. This results in non-time-accurate marching toward a steady-state solution but changes can be convected through the computational domain at much higher speeds than using a single fine grid.

The time-marching procedure begins with an initial guess based on the boundary conditions given in Table 1. The solution procedure over one time step can be broken down into the following stages:

(1) Calculation of gas properties and changes in each primary variable at every cell vertex:
   - At every cell vertex the physical properties of the gas mixture (p, T, μ, λ, Y, D) are calculated from the primary variables.
   - At every cell centre the changes in each primary variable ($(\Delta\rho_i)_{\text{cell}}$, $(\Delta\rho e)_{\text{cell}}$ and $(\Delta\rho\mathbf{U})_{\text{cell}}$) are calculated over a time step Δt_{cell} (based on $\text{CFL} = 8$) using Eqs. (18)–(22).
   - The changes in the cell-vertex values of each primary variable are calculated from a mean of the changes stored at the surrounding cell centres.

(2) Calculation of the pressure using $\text{CFL} = 0.005$:
   - The stored values of ρ_i and ρe are updated using $\text{CFL} = 0.005$ by adding a small fraction of the cell-vertex changes calculated using $\text{CFL} = 8$ in step 1.
   - New values of ρ, Y_i and T are calculated and hence a new value of pressure can be found at every cell vertex.

(3) Calculation of new values of ρ_i and ρe using $\text{CFL} = 8$:
   - ρ_i and ρe are re-updated at every cell vertex by adding the full value of the cell-vertex changes.
   - New values of Y_i and T are calculated.
   - ρ is adjusted to ensure the new value of pressure is identical to the value found in step (2).
   - Final values of ρ_i and ρe are recalculated based on the new values of Y_i and T and the adjusted value of ρ.

(4) Calculation of velocities:
   - $\rho\mathbf{U}$ is updated at every cell vertex by adding the full value of the cell-vertex changes.
   - $\mathbf{U}$ is calculated using the adjusted value of ρ.

(5) The new values of the primary variables are then smoothed using a second-order smoothing algorithm. This is equivalent to adding a small amount of artificial viscosity to the equations.

(6) The boundary conditions are applied.

This process is repeated over many time steps until the converged steady-state solution is attained.

4.2. Physical properties

In step (1) the physical properties of the gaseous mixture are evaluated. The temperature of the gas T is obtained by solving Eqs. (14)–(16). The values of gas viscosity, thermal conductivity and specific heat capacity

are all functions of temperature and composition. For each species, the variation of each property with temperature is defined by a quadratic curve fit to tabulated data [16]. A mole fraction average

$$\mu = \sum_{i=1}^{n} X_i \mu_i \tag{25}$$

is used to obtain an estimate of the viscosity and the thermal conductivity at a given gas composition. Although this method is not the most accurate available, it is computationally cheaper than the methods of Reichenberg and Wassiljewa [16] and was shown to give acceptable accuracy over the range of interest. A mass fraction average is used to predict the value of specific heat capacity for a given gas composition.

4.3. Boundary conditions

At the solid walls, the prescribed boundary values are used to overwrite the variables computed by the numerical procedure. The fluxes normal to the solid walls are set as in Table 1. The mass-averaged velocity is set in conjunction with the diffusion velocity to give the correct total flux of each species. A no-slip boundary condition is applied to the tangential flow along the solid walls. The calculation procedure at the inlet is designed to ensure that the convective and diffusive fluxes are conserved from outlet to inlet and that the flow at the inlet has the correct mean values of $p_{0,\mathrm{m}}$, $T_{0,\mathrm{m}}$ and $X_{i,\mathrm{m}}$.

5. Results

The results presented below are calculated with the conditions given in Section 2 which represent the typical dimensions and operating conditions of an IP-SOFC. Under these conditions it is expected that the flow field is steady and laminar [7] which may not be the case for other designs of fuel cell systems.

5.1. Code validation

Fig. 6 shows calculations of possible streamline patterns for the steady two-dimensional laminar flow through the computational domain for different sized gaps S_x between the bundles. The flow encounters a sudden expansion followed by a sudden contraction and it is expected that regions of recirculation will form between the bundles. In Fig. 6a, S_x is larger than the reattachment length x_r of the region of recirculation that forms behind the back face of the module. The flow therefore sees the next module as a forward-facing step.

The flow over a backward-facing step is of great engineering interest and has been much studied in the last few decades [17–19]. Goldstein et al. [18] measured x_r for different values of Reynolds Number (Re_M) and for a range of step to channel height ratios, see Fig. 7. A comparison is made with results obtained using the present numerical method and the geometry described in this paper. Goldstein et al. [18] used experimental

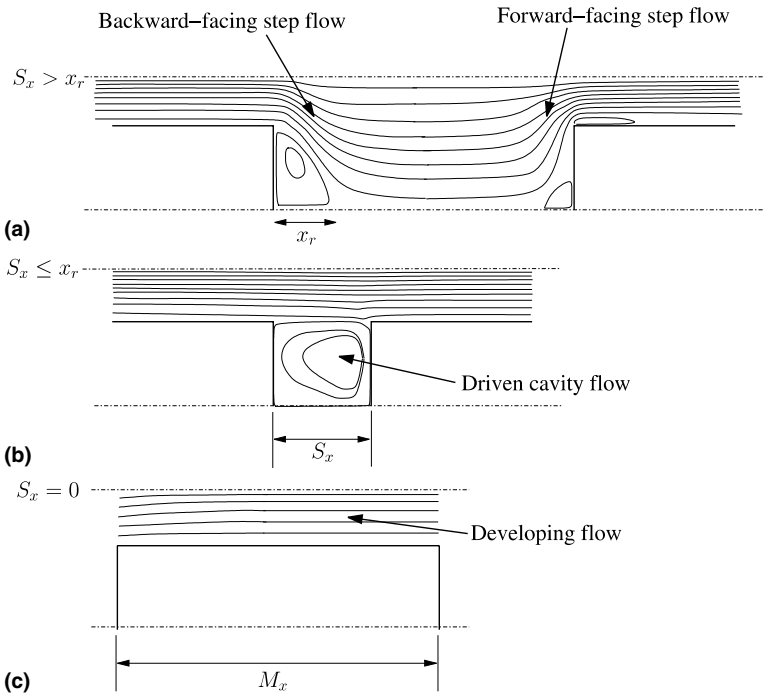

Fig. 6. Calculation of streamline patterns for three possible flow fields.

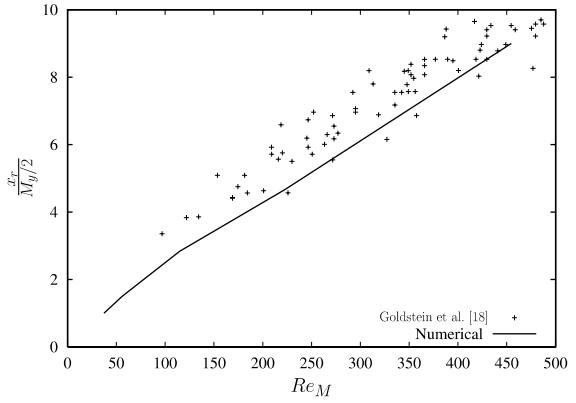

Fig. 7. Variation of horizontal separation length downstream of a backward facing step. A comparison between the experimental results of [18] and the numerical method developed in this paper.

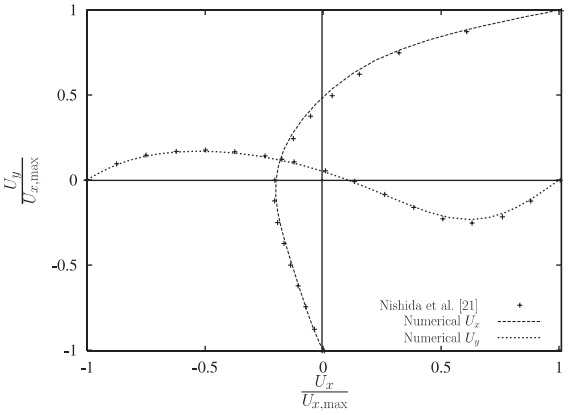

Fig. 8. Normalised velocity profiles for a two-dimensional square lid-driven cavity flow. The velocity profiles perpendicular to and located at both of the two centrelines are plotted. The comparison is between the high-order numerical solution of Nishida et al. [21] and the numerical method described in this paper.

apparatus with a large width to step height ratio in order to observe and measure a two-dimensional flow field. A small secondary flow initiated from the side walls of their experimental apparatus which are not present in the geometry considered in this study. Fig. 7 shows good agreement between the numerical and the experimental results despite the experimental observation of a secondary flow.

In Fig. 6b, the value of S_x is small enough that the region of recirculation that forms behind the back face of the module fills the horizontal gap. This situation is similar to a lid-driven cavity flow where a recirculating flow is driven by fluid shear on the top surface of the cavity. The lid-driven cavity flow is a benchmark in computational fluid dynamics and is often simulated in two dimensions. The agreement between two-dimensional simulations [20–22] and three-dimensional experiments [23–25] is good. Fig. 8 shows the centre-line velocity profiles in a square lid-driven cavity flow at a Reynolds number of 100 (based on the velocity at the lid and the cavity height). A comparison is shown between the high-order numerical method of Nishida et al. [21] and the numerical method described in this paper.

In Fig. 6c, air flows between one pair of modules only, which can be regarded as parallel plates. Heaton et al. [26] solved the governing equations for simultaneously developing velocity and temperature boundary layers between parallel plates subjected to a constant heat flux and found good agreement with their experimental work. In this study the local Nusselt number ($Nu(x)$) on the top surface of a module ($y = 0$) is defined as

$$Nu(x) = \frac{h(x)2S_y}{\lambda_m}, \qquad h(x) = \frac{q_{wall}}{T_{wall} - T_m} \tag{26}$$

where $h(x)$ is the heat transfer coefficient. Fig. 9 shows the variation of $Nu(x)$ along a pair of heated plates, as calculated by Heaton et al. [26]. The analogous mass transfer dimensionless group, the local Sherwood number ($Sh(x)$), is defined as

$$Sh_i(x) = \frac{k_i(x)2S_y}{\rho_m D_m}, \qquad k_i(x) = \frac{g_{i,wall}}{Y_{i,wall} - Y_{i,m}} \tag{27}$$

where $k_i(x)$ is the mass transfer coefficient of species i. For comparison, Fig. 9 shows the variation of $Sh_{O_2}(x)$ and $Nu(x)$ calculated using the method and the heat

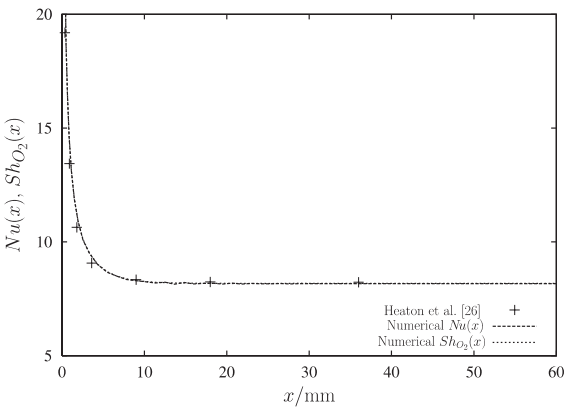

Fig. 9. Variation of $Nu(x)$ and $Sh_{O_2}(x)$ along the length of a module for a developing flow. A comparison is made between the solution for $Nu(x)$ of Heaton et al. [26] and the variation of $Nu(x)$ and $Sh_{O_2}(x)$ calculated using the method described in this paper.

and mass transfer boundary conditions described in this paper. It can be seen that, for the small level of 'wall suction' occurring in this study, the analogy between heat and mass transfer can be made successfully. The entry length is 15 mm for the thermal and diffusion boundary layers and the hydrodynamic entry length (not shown) is rather less at 10 mm.

5.2. Test cases

The test cases presented here are chosen to illustrate the effect of varying the horizontal gap S_x between bundles. The same boundary conditions, given in Section 2, are used for each test case. S_x is varied from 5 mm to 25 mm in 10 mm intervals. A convergence study was performed for the test case where $S_x = 5$ mm to confirm that the code converges to a solution and to identify the grid spatial resolution required. This test case was simulated on four successively finer grids, the total number of grid cells doubling from one test to the next. Fig. 10 shows the calculated variation of $Nu(x)$ near the leading edge of the module for the four grids and suggests that a grid containing 18 000 cells gives an accurate result. Fig. 11 shows this computational grid and the number of cells in the x and y-directions. No variation in flow properties is expected in the z-direction and hence a coarse grid comprising only 4 cells is used in that direction. There are high concentrations of grid cells around the corners of the module to deal with the flow field singularities which occur at those locations. All the results are plotted in an x–y plane located at $z = L_z/2$ as in Fig. 4.

For each of the three test cases ($S_x = 5$, 10, 15 mm), the simulation took about 80 min of CPU time to converge on a 1.5 GHz Pentium 4 PC. The numerical solutions are obtained for $Re_S = 100$ and $Re_M = 50$ for all the test cases and, as shown above, the entry lengths of the air flow are of the order of 10 mm. Therefore, the contour plots described below are focused on the gap between bundles where the flow is undeveloped.

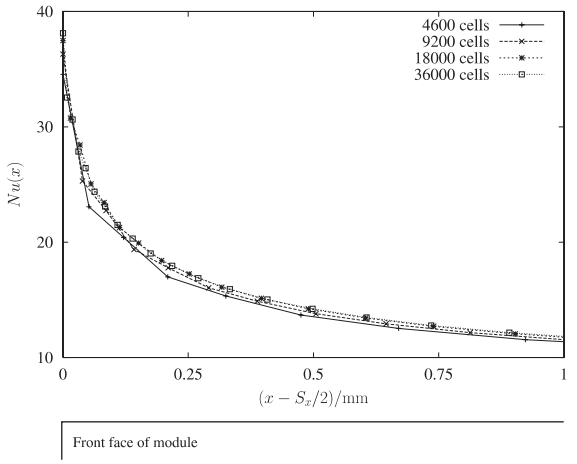

Fig. 10. Variation of the calculated value of $Nu(x)$ near the leading edge of a module for four successively finer computational grids.

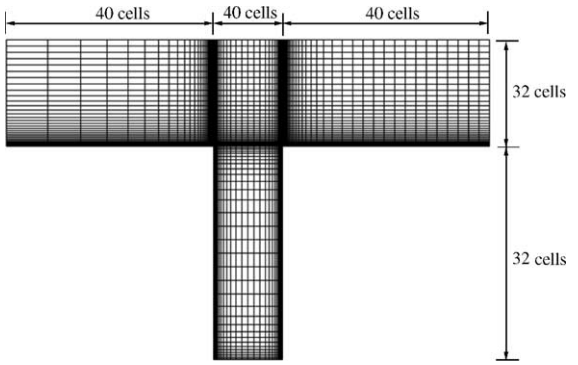

Fig. 11. The computational grid in the x–y plane (not to scale).

Fig. 12 shows the air flow streamlines for the three different gap sizes. As S_x increases, the flow regime

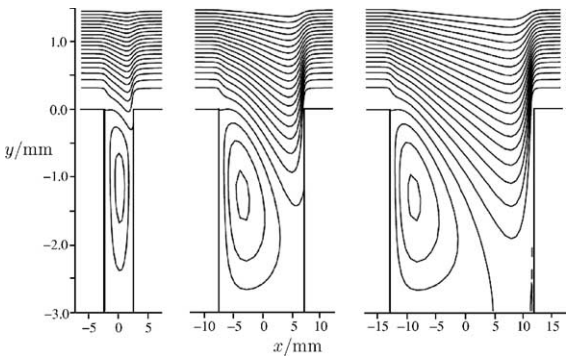

Fig. 12. Streamline plots for increasing inter-bundle gap spacing. The x and y axes are plotted on different scales.

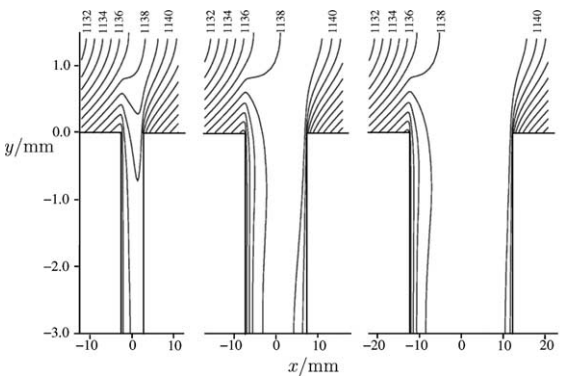

Fig. 13. Contours of constant temperature T (K) for the same conditions as in Fig. 12.

exhibits a transition from a flow similar to a driven cavity flow to a backward/forward-facing step flow. Fig. 13 shows contours of constant temperature for the three test cases. As mentioned above, the gaps between bundles S_x break up and flatten the profiles of the boundary layers that form on the top surface of each module. The flattening of the thermal boundary layer profile is caused by recirculation and conduction in the flow between bundles and is more effective with larger S_x. The thermal boundary layer develops over a short distance from leading edge of the module top surface and once fully-developed its shape is unchanging over the rest of the module surface. In the vicinity of the back face of the module the sudden expansion of the flow into the gap between bundles changes the shape of the thermal boundary layer profile slightly.

Fig. 14 shows the calculated variation of $Nu(x)$ on the top face of the module in the regions near the front and back faces and a comparison with the variation of $Nu(x)$ for a developing flow between parallel plates, as shown in Fig. 9. Fig. 14 shows that the value of $Nu(x)$ at the front of a module rises with increasing S_x as the temperature profile at $x = S_x/2$ moves closer to a flat profile. However, this temperature profile is not totally flat and hence $Nu(x)$ is lower than the infinite value at the leading edge of a developing flow between parallel plates. The value of $Nu(x)$ decreases as the thermal boundary layer develops and it remains at a constant value of 8.24 where the thermal boundary layer is fully-developed. $Nu(x)$ increases slightly in the region near the back face of the module because of the sudden expansion mentioned above.

Fig. 13 shows that S_x does have an effect on the heat transfer from the front and back faces of the module. Fig. 15 shows the variation of $Nu(x, y)$ on these faces. $Nu(x, y)$ is defined as

$$Nu(x,y) = \frac{h(x,y)2S_x}{\lambda_{\text{wall}}}$$
$$h(x,y) = \frac{q_{\text{wall}}}{T_{\text{wall}} - T_s} \tag{28}$$

where $2S_x$ is the hydraulic diameter of parallel plates with a separation S_x and T_s is the free-stream temperature (which is defined as the temperature at $x = 0$ for any given y coordinate). There is an improvement in heat transfer with increasing S_x and toward the corners of the module ($y = 0$). As expected, $Nu(S_x/2, y)$ is higher

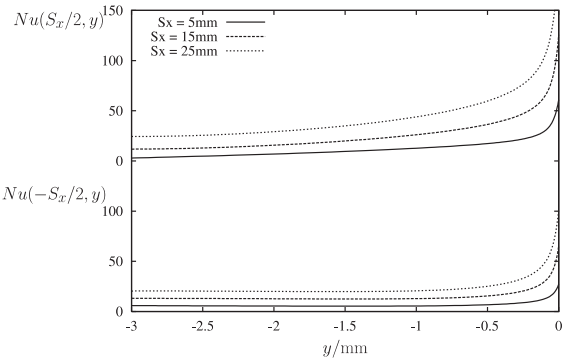

Fig. 15. Variation of Nu along the front face ($x = S_x/2$) and back face ($x = -S_x/2$) of the module for different values of S_x.

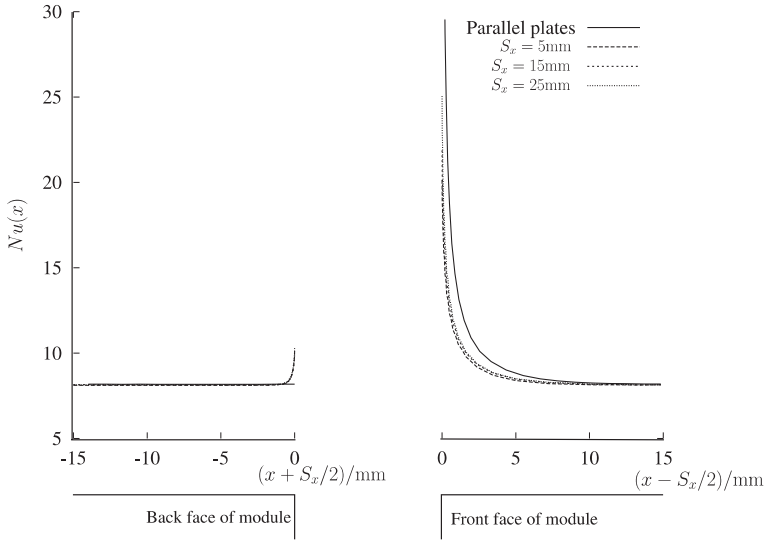

Fig. 14. Variation of $Nu(x)$ along the length of a module for the three test cases. A comparison is made between the solution for $Nu(x)$ for a developing flow between parallel plates as shown in Fig. 9.

than $Nu(-S_x/2, y)$ due to the higher local air speed. The overall temperature rise across a module is 30 K and is independent of S_x.

Fig. 16 shows contours of constant oxygen mole fraction X_{O_2} for the three test cases. The distribution of X_{O_2} is very similar to the distribution of temperature shown in Fig. 13. Indeed, the analogy between heat and mass transfer suggests that the two distributions should be almost identical. Fig. 17 shows the calculated variation of $Sh_{O_2}(x)$ along the top face of the module. The behaviour of $Sh_{O_2}(x)$ is much closer to the parallel plate model than is the behaviour of $Nu(x)$. The gap between bundles improves the mass transfer more than the heat transfer at the leading edge of the module. This difference is caused by the non-adiabatic heat flux boundary conditions on the front and back faces of the module, see Table 1, which decrease the flattening effect that the gap between bundles has on the thermal boundary layer profile. For all test cases the total decrease in X_{O_2} is 0.0042 which is small enough to have a negligible effect on fuel cell performance.

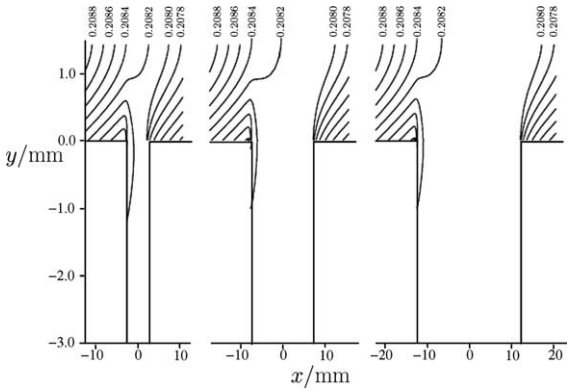

Fig. 16. Contours of constant oxygen mole fraction X_{O_2} for the same conditions as in Fig. 12.

6. Conclusions

A numerical method for solving the steady laminar low Mach number air flow within a three-dimensional array of IP-SOFC modules has been described. This method is straightforward to implement and has the accuracy required to capture the two-dimensional flow field over a complicated geometry containing singularities. The numerical scheme uses a simplified 'preconditioning' technique that can be applied to flows with large variations in physical properties. The gap between bundles causes a flattening of the boundary layer profiles which has a positive effect on the heat and mass transfer at the leading edge of each module. This improvement is limited because at IP-SOFC operating conditions all the boundary layers are fully-developed a short distance from the leading edge of the module. The results show how differing heat and mass flux boundary conditions lead to a greater improvement in mass transfer on the module surface. The overall change in oxygen mole fraction is negligible and it is the cooling effect of the air flow through the bundles that is of great importance in the design of the IP-SOFC.

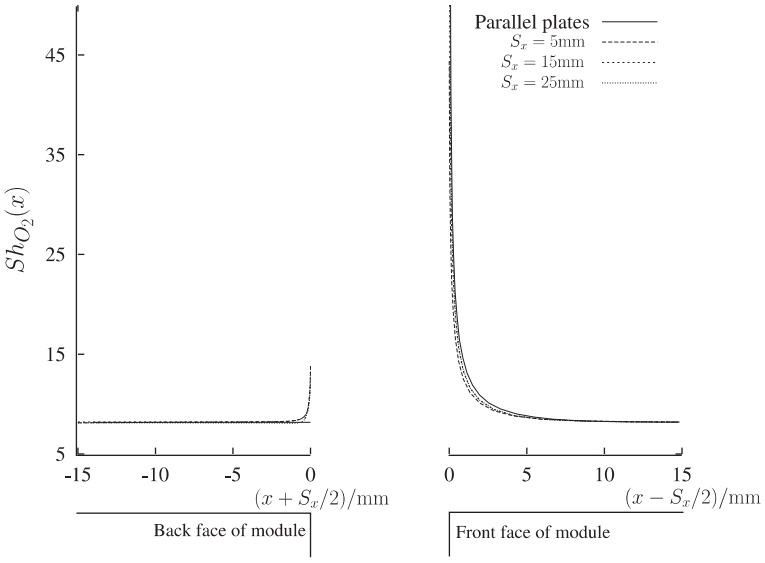

Fig. 17. Variation of $Sh_{O_2}(x)$ along the length of a module for the three test cases. A comparison is made with the solution for $Sh_{O_2}(x)$ for the developing flow between parallel plates.

Acknowledgements

Mr B. Haberman was supported by an EPSRC research studentship and a Rolls-Royce CASE award. The authors are indebted to Prof. J.D. Denton of the Whittle laboratory, University of Cambridge for generously making available his time-marching computer program for turbomachinery flows. They are also grateful for the technical assistance supplied by the staff of Rolls-Royce Fuel Cell Systems Ltd., particularly Dr. G. Agnew and Mr. R. Collins.

References

[1] F.J. Gardner, M.J. Day, M.P. Brandon, M.N. Pashley, M. Cassidy, SOFC technology development at Rolls-Royce, J. Power Sources 86 (2000) 122–129.
[2] W.M. Kays, M.E. Crawford, Convective Heat and Mass Transfer, McGraw-Hill, New York, 1987.
[3] O. Leon, G. De Mey, E. Dick, Study of optimal layout of cooling fins in forced convection cooling, Microelectron. Reliab. 42 (2002) 1101–1111.
[4] W.M. Kays, A.L. London, Compact Heat Exchangers, second ed., McGraw-Hill, 1964.
[5] S.V. Patankar, C. Prakash, An analysis of the effect of plate thickness on laminar flow and heat transfer in interrupted-plate passages, Int. J. Heat Mass Transfer 24 (1981) 1801–1810.
[6] L.W. Zhang, S. Balachandar, D.K. Tafti, F.M. Najjar, Heat transfer enhancement mechanisms in inline and staggered parallel-plate fin heat exchangers, Int. J. Heat Mass Transfer 40 (1997) 2307–2325.
[7] L.W. Zhang, D.K. Tafti, F.M. Najjar, S. Balachandar, Computations of flow and heat transfer in parallel-plate fin heat exchangers on the CM-5: effects of flow unsteadyness and three-dimensionality, Int. J. Heat Mass Transfer 40 (1997) 1325–1341.
[8] B.A. Haberman, J.B. Young, Three-dimensional simulation of chemically reacting gas flows in the porous support structure of an integrated-planar solid oxide fuel cell, Int. J. Heat Mass Transfer 47 (August) (2004) 3617–3629.
[9] C.L. Merkle, Y.H. Choi, Computation of low-speed compressible flows with time marching procedures, Int. J. Numer. Methods Fluids 25 (1988) 293–311.
[10] M. Sabanca, G. Brenner, N. Alemdaroglu, Improvements to compressible Euler methods for low-Mach number flows, Int. J. Numer. Methods Fluids 34 (2000) 167–185.
[11] J.M. Weiss, W.A. Smith, Preconditioning applied to variable and constant density flows, AIAA J. 33 (1995) 2050–2056.
[12] R.M. Gatiganti, K.J. Badcock, F. Cantariti, L. Dubuc, M. Woodgate, B.E. Richards, Evaluation of an unfactored method for the solution of the incompressible flow equations using artificial compressibility, Appl. Ocean Res. 20 (1998) 179–187.
[13] C.-H. Li, R. Glowinski, Modelling and numerical simulation of low-Mach-number compressible flow, Int. J. Numer. Methods Fluids 23 (1996) 77–103.
[14] D. Kwak, S. Chakravarthy, A three-dimensional incompressible Navier–Stokes flow solver using primitive variables, AIAA J. 24 (1986) 390–396.
[15] J.D. Denton, The calculation of three-dimensional viscous flow through multistage turbomachines, ASME J. Turbomach. 114 (1992) 18–26.
[16] B. Todd, J.B. Young, Thermodynamic and transport properties of gases for use in solid oxide fuel cell modelling, J. Power Sources 110 (2002) 186–200.
[17] D. Barkley, M. Gabriela, M. Gomes, R.D. Henderson, Three-dimensional instability on flow over a backward-facing step, J. Fluid Mech. 473 (2002) 167–190.
[18] R.J. Goldstein, V.L. Eriksen, R.M. Olson, E.R.G. Eckert, Laminar separation, reattachment and transition of the flow over a downstream-facing step, ASME J. Basic Eng. 92 (1970) 732–741.
[19] B.F. Armaly, F. Durst, J.C.F. Pereira, B. Schonung, Experimental and theoretical investigation of backward-facing step flow, J. Fluid Mech. 127 (1983) 473–496.
[20] A. Abouhamza, R. Pierre, A neutral stability curve for incompressible flow in a rectangular driven cavity, Math. Comput. Modell. 38 (2003) 141–157.
[21] H. Nishida, N. Satofuka, Higher-order solutions of square driven cavity flow using a variable-order multi-grid method, Int. J. Numer. Methods Eng. 34 (1992) 637–653.
[22] J. Zhang, Numerical simulation of 2D square driven cavity using fourth-order compact finite difference schemes, Comput. Math. Appl. 45 (2003) 43–52.
[23] J.R. Koseff, R.L. Street, The lid-driven cavity flow: a synthesis of qualitative and quantitative observations, ASME J. Fluids Eng. 106 (1984) 390–398.
[24] J.R. Koseff, R.L. Street, Visualization studies of a shear driven three-dimensional recirculating flow, ASME J. Fluids Eng. 106 (1984) 21–29.
[25] J.R. Koseff, R.L. Street, On end wall effects in a lid-driven cavity flow, ASME J. Fluids Eng. 106 (1984) 385–389.
[26] H.S. Heaton, W.C. Reynolds, W.M. Kays, Heat transfer in annular passages. Simultaneous development of velocity and temperature fields in laminar flow, Int. J. Heat Mass Transfer 7 (1964) 763–781.